Geomechanics and Engineering, *Vol. 29, No. 2 (2022) 193-205*
https://doi.org/10.12989/gae.2022.29.2.193

Visualization analysis of the progressive failure mechanism of tunnel face in transparent clay

Huayang Lei[1,2a], Saibei Zhai[1,3b], Yingnan Liu*[1] and Rui Jia[1,2c]

[1]*Department of Civil Engineering, Tianjin University, Tianjin, China 300072*
[2]*Key Laboratory of Coast Civil Structure Safety of Education Ministry, Tianjin University, Tianjin, China 300072*
[3]*Beijing Urban Construction Design & Development Group Co., Ltd., 5 Fuchengmen North Street, Beijing, China 100032*

(Received September 15, 2020, Revised March 14, 2022, Accepted March 19, 2022)

Abstract. The face stability of shield tunnelling is the most important control index for safety risk management. Based on the reliability of the transparent clay (TC) model test, a series of TC model tests under different buried depth were conducted to investigate the progressive failure mechanism of tunnel face. The support pressure was divided into the rapid descent stage, the slow descent stage and the basically stable stage with company of the local failure and integral failure in the internal of the soil during the failure process. The relationship between the support pressure and the soil movement characteristics of each failure stage was defined. The failure occurred from the soil in front of the tunnel face and propagated as the slip zone and the loose zone. The fitted formulas were proposed for the calculation of the failure process. The failure mode in clay was specified as the basin shape with an inverted trapezoid shape for shallow buried and appeared as the basin shape with a teardrop-like shape in deep case. The implications of these findings could help in the safety risk management of the underground construction.

Keywords: failure mechanism; soil deformation; transparent clay; tunnel face

1. Introduction

The prominent problems brought by the acceleration of urbanization are traffic congestion and the shortage of urban land. The development of underground space, via predominantly shield tunnelling construction, has become mainstream. Meanwhile, the safety of underground construction, especially in complex urban environments and varied stratigraphic conditions, has become a hot issue in recent years (Alagha *et al.* 2019, Azadi *et al*. 2020). The analysis of the face stability of shield tunnelling is the most important control index for safety risk management.

Due to the high cost of field tests, most studies rely on physical modelling and numerical simulations to understand different phenomena related to tunnelling, such as the deformation patterns and failure mechanisms. Because of the opacity of the soil, failure mechanisms were obtained by observing the microscopic deformations at the transparent boundary of semi-tunnel model tests (Kimura and Mair 1981, Nomoto *et al*. 1999, Kamata and Mashimo 2003, Shin *et al*. 2008, Juneja *et al*. 2010, Kirsch 2010, Berthoz *et al*. 2012, Chen *et al.* 2013, Kim *et al.* 2016, di Prisco *et al*. 2018b, Lv *et al.* 2018, Li *et al*. 2021), the internal deformation of soil can't be observed through these traditional test methods. Meanwhile, almost all conventional model tests are conducted in sand, owing to the complex and variable properties of clay. In addition, clay easily adheres to the transparent boundary, which hinders the deformation of the soil and interferes with the measurement of the soil deformation. Thus, the actual soil deformation may not be fully reflected due to the boundary conditions. Furthermore, internal soil deformations measured by sensors buried in soils would inevitably influence the behaviour of the soils and lead to test data distortion. Therefore, the main concern of the previous study focused on the failure mode in sand layers, there are few model tests related to clay layers, the face failure evolution process and the failure mechanism of tunnel face deserve further study. Numerical simulations associated with reliability-based design (di Prisco *et al*. 2018a, Eskandari *et al.* 2018, Li *et al*. 2019a, Sahoo and Kumar 2019, Xue *et al.* 2019, Senent *et al*. 2020, Fernandez *et al*. 2021) are another common method used in face stability research, but there is great uncertainty in the parameter selection.

Transparent soils make it possible to visualize the flow paths and deformations inside of soil, providing a good way to overcome these problems. It is made of transparent particles whose geotechnical properties are similar to natural soil and a pore liquid with a matched refractive index. (Iskander 2010, Lei *et al*. 2019, Wang *et al*. 2021). Currently, it has been used to achieve the three-dimensional (3D) visualization of geotechnical problems, especially in the study of shallow foundations and pile penetration (Guzman *et al*. 2018, Ads *et al*. 2020, Zhang *et al*. 2020a, c).

*Corresponding author, Ph.D. Student
E-mail: lyn1996@tju.edu.cn
[a]Professor
E-mail: leihuayang74@163.com
[b]Master
E-mail: beichenstyle@foxmail.com
[c]Associate Professor
E-mail: jiarui@tju.edu.cn

ISSN: 2005-307X (Print), 2092-6219 (Online)

Transparent soils have also been used to study tunnel failure mechanisms. Ahmed (2011, 2012) used transparent soil model tests to study the tunnel face stability by reducing the support pressure and found that the failure was a sudden process and the ultimate failure formed a prismatic wedge around the tunnel and a vertical chimney near the ground. Sun *et al.* (2014) found that the failure shape ahead of the tunnel face could be divided into two parts: the shape of the lower part remained an inverted trapezoid, but the shape of the upper part propagated from a rectangle to a bell over a trapezoid as the buried depth propagated from shallow to deep. Xiang *et al.* (2018) proposed that the failure mode maintained a funnel shape with the decrease in the surrounding material strength but propagated from the funnel shape to a chimney shape with the increase in the buried depth. Zhang *et al*. (2020b) stated the predictive equations with regard to the ground loss ratio and the vertical and horizontal displacements of a single tunnel considering different ground loss ratios. Owing to the high requirement of material purity and particle size, the complexity of the sample preparation process, and the difficulty of controlling the maximum optimum transparency, the vast majority of the previous study of transparent soils are carried out in transparent sand layers, there are relatively few studies on the model tests via transparent clay. Meanwhile, the tunnel face failure mechanism and the failure mode in clay layers have not been systematically studied.

In this paper, the displacement-controlled method was used to carry out a series of transparent clay model tests under different buried depths (C/D=0.5, 1.0 and 2.0) and different profiles (longitudinal and cross). On the basis of verifying the reliability of transparent clay model test, the propagation process of the internal soil during the whole failure process was analysed and the failure mechanism in clay was defined. The distinction of the failure mechanism in clay and sand layers was compared and specified, which could provide meaningful conclusions for underground construction.

2. Transparent soil model test

2.1 Transparent soils

The transparent material used in this study was prepared by mixing amorphous silica powder (by Lianyungang Hongding Fused Quartz Co., Ltd.) with a mix of White Oil No.15 (by Hainan Handi Sunshine Patrochemical Co., Ltd.) and N-Dodecane (by Tianjin Kemiou Chemical Reagent Co., Ltd.), which have the same refractive index. As shown in Fig. 1, the particle size distribution curves of transparent clay and natural clay (Horpibulsuk *et al.* 2013, Lei *et al.* 2018) show a good similarity when particle size is more than 10 μm, and it is an ideal material for modelling natural clay.

The mixed liquid of White Oil No.15 and N-Dodecane is widely used as a pore liquid (Xiang *et al.* 2018, Kong *et al.* 2018, Liu *et al*. 2021). The two liquids were mixed homogeneously, and then a certain mass of silica powder

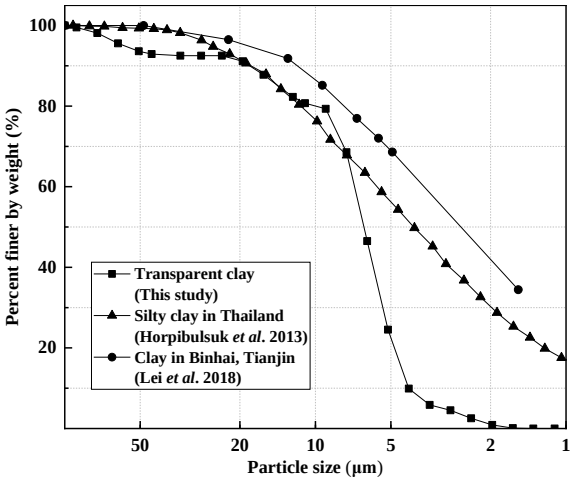

Fig. 1 Particle size distribution curve

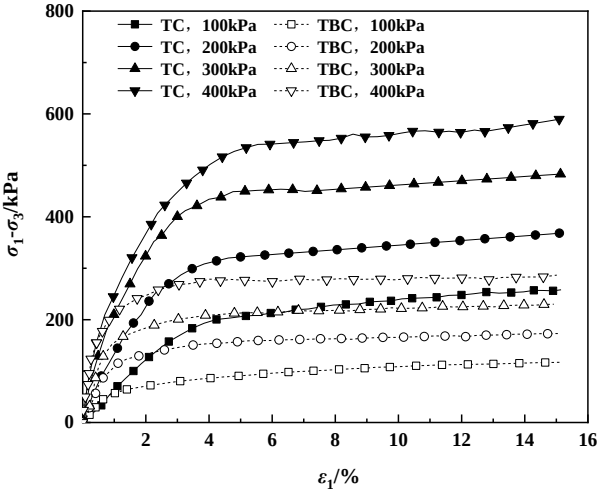

Fig. 2 The results of the CU shear tests

was uniformly added into the pore liquid and mixed. During this process, a glass rod was used to stir the mixture continuously. Finally, a vacuum process was conducted to de-air the mixture. After a series of trail-and-error tests to achieve the best transparency, the final volume ratio of the White Oil No.15 and N-Dodecane was 10:3, and the final mass ratio of the pore liquid and silica powder was 150% at a temperature of 20±1°C. The maximum optimum transparency was tested and could reach 15cm, which was sufficient for the transparent model test.

The geotechnical properties of the transparent clay used in this study with the clay used by other studies (Mohidin *et al.* 2010, Horpibulsuk *et al.* 2013, Li 2017, Lei *et al.* 2018) are compared in Table 1. The density of TC is relatively close to TC-M but smaller than that of the natural clay, due to the low density of silica powder. Compared with TC-M introduced by Mohidin *et al.* (2010), TC has a good similarity in compression index and friction angle to natural silty clay TBC, which satisfies the geotechnical properties better. The coefficient of permeability of TC is within the scope of TBC and slightly less than that of TC-M, which belongs to the normal variation range of transparent clay (Iskander *et al*. 2002). The consolidated undrained (CU)

Table 1 Basic geotechnical properties

Soil	Density, ρ (g/cm^3)	Water(oil) content, ω (%)	Compression index, C_c	Friction angle, φ (°)	Cohesion, c (kPa)	Coefficient of permeability, k (m/s)
THC*	1.79	98.0	-	-	1.5	-
TBC	1.757	50.3	0.65	9.3	17.6	1.0×10^{-9}~1.0×10^{-6}
FMC	1.85	61.4	-	6	0.6	-
TC-M	1.30 (-17.5%)	-	3.8~4.6 (484.6%~607.7%)	34 (265.6%)	-	8.5×10^{-6}~9.5×10^{-6}
TC	1.08 (-31.4%)	150 (198.2%)	0.543 (-16.5%)	14.19~18.65 (52.6~100.5%)	11.7~22.62 (-33.5%~28.5%)	1.4×10^{-7}~3.5×10^{-6}

THC*: Clay in Thailand (Horpibulsuk *et al.* 2013); TBC: Silty clay in Binhai, Tianjin (Lei *et al.* 2018); FMC: Flowing mud clay in Hangzhou, China (Li 2017); TC-M: Transparent clay (Mohidin *et al.* 2010); TC: Transparent clay (This study)

shear tests were conducted with confining pressures of 100 kPa, 200 kPa, 300 kPa and 400 kPa to compare the stress-strain behaviour of TC and TBC, the results for the CU were shown in Fig. 2. The development trend of stress-strain curves of TC and TBC are basically the same, which appears to increase first and then keep stabilizing. The consolidated undrained strength of TC is about twice that of TBC. Therefore, to a certain extent, it reflects that the stiffness of the two kinds of clay roughly conforms to the linear similarity.

Therefore, the properties of the TC used in the model test could be verified. The detailed geotechnical properties of TC used in this study are reported by Lei *et al.* (2019).

2.2 Test apparatus

The model test apparatus used in this study is illustrated in Fig. 3 and includes an optical platform, liner guides, a transparent platform, a transparent model box, a transparent cover, an optical laser, a black light-shielding curtain, tracer particles, a black and white charge-coupled device (CCD) camera, a pressure-measuring device and PIVview2C software.

This optical platform and the black light-shielding curtain can avoid outside interference in the model tests. The liner guides, transparent platform and vacuum pump can be used for convenient slicing of the model. The vacuum pump is used to de-air the TC sample in the vacuum process. The tracer particles used in this study are hollow glass microspheres named iM16K (manufactured by 3M^{TM}, St. Paul, USA), which have a high degree of recognition when irradiated with an optical laser. The internal displacement field of the soil could be represented by the movement of tracer particles, whose particle size is 9~25 μm. Since the particle size of the tracer particles is basically the same as that of amorphous silica powder, it will not affect the mechanical properties of the TC.

A sketch of the transparent Plexiglas acrylic model box is shown in Fig. 4. The inner dimensions of the box are 25×25×40 cm^3 (length× width× height). A polished black aluminium pipe protrudes into the model box 13 cm to model the tunnel. The supporting plate can draw back 1.5 mm when the screw nut rotates in a complete circle. A sketch of the transparent Plexiglas acrylic cover is shown in Fig. 5. The vacuum process could be controlled by the suction valve and the vacuum pressure could be measured by the vacuum manometer.

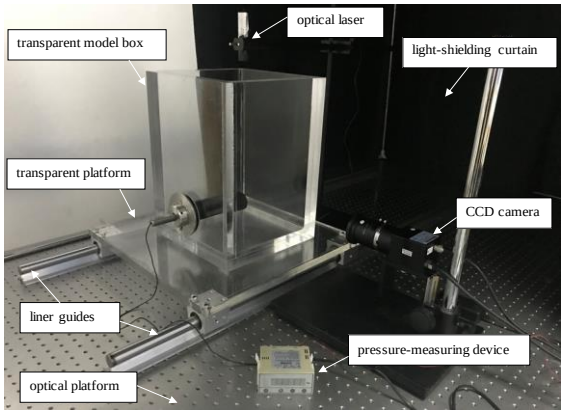

Fig. 3 Test apparatus of the experimental model

The optical laser, CCD camera, pressure-measuring device and PIVview2C software are used for digital image and data processing. The optical laser, with an output power of 200 mW, is used to generate a clear speckle slice inside the TC sample. The resolution of MV-E1600M CCD camera is 4896×3264 pixels, 20 cm from the transparent platform, used to capture images during failure process. A macro lens with a resolution of 40 lp/mm (10 MP) is mounted on the CCD camera. The pressure-measuring device is used to record the face support pressure during the failure process. PIVview2C software, which can analyse the images captured by CCD before and after deformation, is used in this study to value the internal soil deformation represented by the tracker particles. The parameters of the windows size (32×32 pixels), step size (16×16 pixels) and optional calculations (4 times) are considered to determine the processing speed and result precision during image sampling. The range of the contour map is set to 0~3.0 mm, mainly to reveal the entire soil displacement field.

The model test apparatus can realize precise control of the failure process. With the rotation of the screw nut, the supporting plate could go forward and backward without rotating, which is more practical in actual construction. Through the gradual retreat of the tunnel face, the support pressure of the tunnel face and the internal soil deformation under each retreat displacement could be continuously captured via this non-contact approach. The test apparatus itself has good airtightness, so the vacuum process was performed directly in the model box, avoiding the further disturbance of the TC sample caused by the movement of

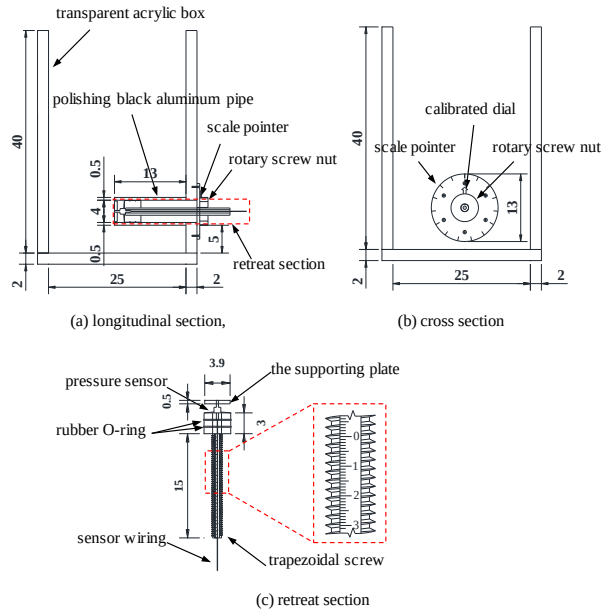

Fig. 4 Sketch of the model test (unit: cm)

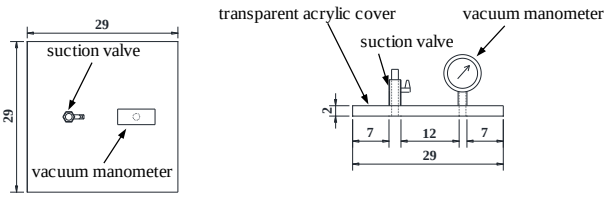

Fig. 5 Sketch of the model cover (unit: cm)

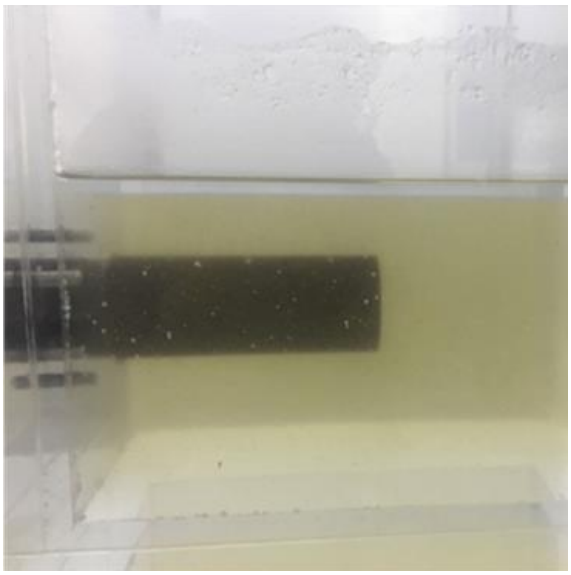

Fig. 6 The transparency of the TC sample

Table 2 Test scheme

Test ID	*C/D*	Profile
1	0.5	longitudinal
2	0.5	cross
3	1.0	longitudinal
4	1.0	cross
5	2.0	longitudinal
6	2.0	cross

the model box after the vacuum process. In the model test, the boundary of the model box was smeared with petroleum jelly to reduce the bonding between the TC sample and the box boundary, thereby greatly reducing the boundary effect.

2.3 Test procedure

The TC sample preparation was conducted in a separate container for convenience. It must be noted that tracker particles were uniformly distributed in the pore liquid, after that the amorphous silica powder was added to ensure the uniform distribution of tracker particles. After mixing, the TC sample became a “mud mass”. Then layers of 5 cm thickness were filled and leveled up into the model box hierarchically. Vaseline was daubed on the top of the model box, and the model cover was placed, these components adhered tightly under negative pressure. The vacuum process was carried out over 60 minutes, in which the air bubbles emerging from the sample disappeared gradually. After the vacuum process, the model box was stood for over 60 minutes, the remaining non-discharged bubbles would "hide" in the soil sample and the black tunnel appeared clearly, as shown in Fig. 6. The model cover was removed, and the soil surface was levelled. The model box would stand for no less than 2 days at a temperature of 20±1℃ for the consolidation process. The geotechnical properties of TC sample were basically consistent to those of natural clay via sample tests.

The model plate and the optical laser were adjusted to form a thin vertical sheet of laser-generated light across the tunnel profile. The light-shielding curtain was closed to keep other light out. In the dark, a speckle field formed, and images were captured by the CCD camera. The screw nut was rotated to control the retreat distance of the supporting plate to 0.75 mm (0.05 mm/s, 15s) each time for each step. After the retreat, the standing time should not be less than 60s to fully stabilize the soil displacement, which could be regarded as the drained soil conditions (Vermeer *et al.* 2002). Until the soil displacement was stable, the laser spot pattern were captured by the CCD camera and the failure process was recorded. A series of digital images was taken, and the support pressure was measured during the failure process.

The test programme is shown in Table 2, where *C* is the cover depth of the tunnel and *D* is the diameter of the tunnel. The changing process of the support pressure and internal soil deformation on the different profiles under different *C*/*D* ratios were studied in this study. For example, after Test 1, the screw nut was rotated to the initial position. The TC sample used in Test 1 was recycled. Stirred the sample fully, the soil was in a loose state and it could be regarded as the sample preparation stage. Then, the vacuum process and the standing process were carried out, same as Test 1. As the soil strength was mainly improved by the vacuum process and the standing time, the soil sample was considered undisturbed.

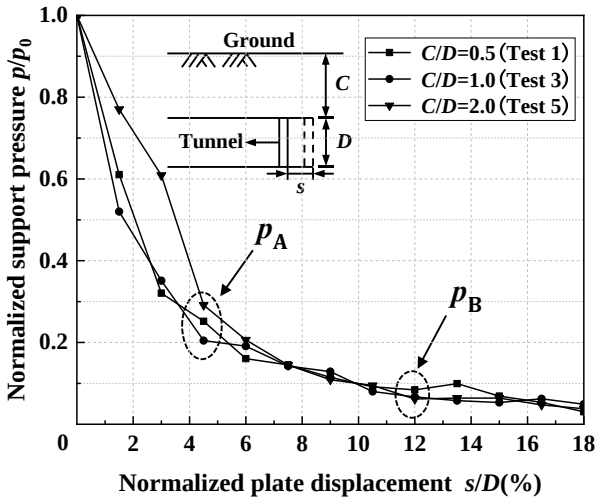

Fig. 7 Normalized support pressure and displacement curves

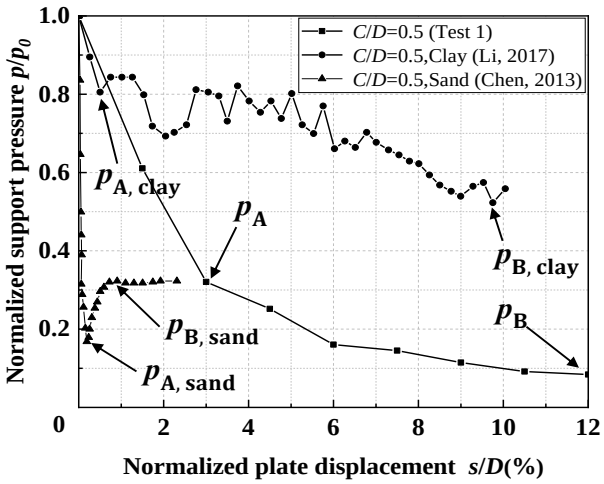

Fig. 8 Comparison of normalized support pressure and displacement curves

3. Results and discussion

3.1 Support pressure and displacement curves

The change stage of the support pressure can reflect the failure state of the soil (Kamata and Mashimo 2003, Zhang *et al*. 2010). Fig. 7 shows the relationship of the normalized support pressure p/p_0 and normalized retreat distance of the supporting plate s/D under different C/D ratios, where s is the retreat distance of the supporting plate, p is the support pressure of the tunnel face during the failure process, and p_0 is the initial pressure on the tunnel face.

As shown in Fig. 7, the changing process of the support pressure could be divided into three stages.

(1) Rapid descent stage ($0<s/D<4.5\%$). With the retreat of the supporting plate, the support pressure decreased steeply. When s/D=4.5%, the support pressure curve of each C/D ratio showed an obvious inflection point, p_A, called the limit support pressure. The results of previous model tests conducted in sand layers (Kirsch 2010, Chen *et al.* 2013) indicated that the limit support pressure would not vary with the buried depth when $C/D\geq1.0$. The results of this study indicate a similar conclusion. The ultimate normalized support pressure of p_A/p_0 was approximately 0.2~0.3.

(2) Slow descent stage ($4.5\%<s/D<12\%$). As the supporting plate continued to retreat, the rate of decrease in the support pressure clearly tended to slow. In this stage, the slope of the support pressure curve remained the same under each C/D. When s/D=12%, the support pressure reached the second critical point, p_B, which was called the residual support pressure. The ultimate normalized support pressure of p_B/p_0 was approximately 0.08.

(3) Basically stable stage ($s/D>12\%$). With the retreat of the supporting plate, the support pressure tended to be stable. In this stage, the normalized support pressure p/p_0 remained approximately 0.08.

According to the above analysis results, the ultimate normalized support pressure of p_B/p_0 under different C/D ratios is basically the same, about 0.08.

Table 3 Comparation of the critical points during the failure process (C/D=0.5)

Reference	soil	s_A/D (%)	p_A/p_0	s_B/D (%)	p_B/p_0
This study	clay	4.5	0.251	12.0	0.084
Li (2017)	clay	3.0	0.805	9.8	0.523
Chen *et al.* (2013)	sand	0.199	0.065	0.946	0.125

Fig. 8 compares the normalized support pressure p/p_0 and normalized retreat distance of the supporting plate s/D with the model tests conducted by Li (2017) for the case of C/D=0.5. The results in sand layers conducted by Chen *et al*. (2013) is also listed in order to compare the changing process of the support pressure in different layers. The changing stages of the support pressure curves in this study and the study of Li (2017) show good consistency, with a similar rapid descent stage and slow descent stage, but there is a big difference in the value of the support pressure, the reason may be that the cohesion of the clay (Li 2017) is too low (only 0.6 Pa), and with the retreat of the supporting plate, the clay accumulated on the tunnel face and the transparent boundary of model box, resulting in a large support pressure. The retreat distance of the supporting plate in this study is much larger than that in sand in the first two stages. The reason for this difference may be the scaling effect. The complex and variable properties of the soil used in different model tests cannot be negligible. In addition, the changing process of the support pressure in clay is clearly more sluggish than that in sand, for example, when the support pressure reached the residual support pressure ($p_{A,sand}$) in sand, the support pressure even not reached the limit support pressure (p_A) in clay. The support pressure curve for sand has a slowly rising process after the rapid descent stage, due to the dilatancy of the sand. But for clay, there is a slow descent stage instead. This is because the shear strength of clay is less than that of sand.

Table 3 summarizes the critical displacement points of this study and the studies of Chen *et al.* (2013) and Li (2017) for the case of C/D=0.5.

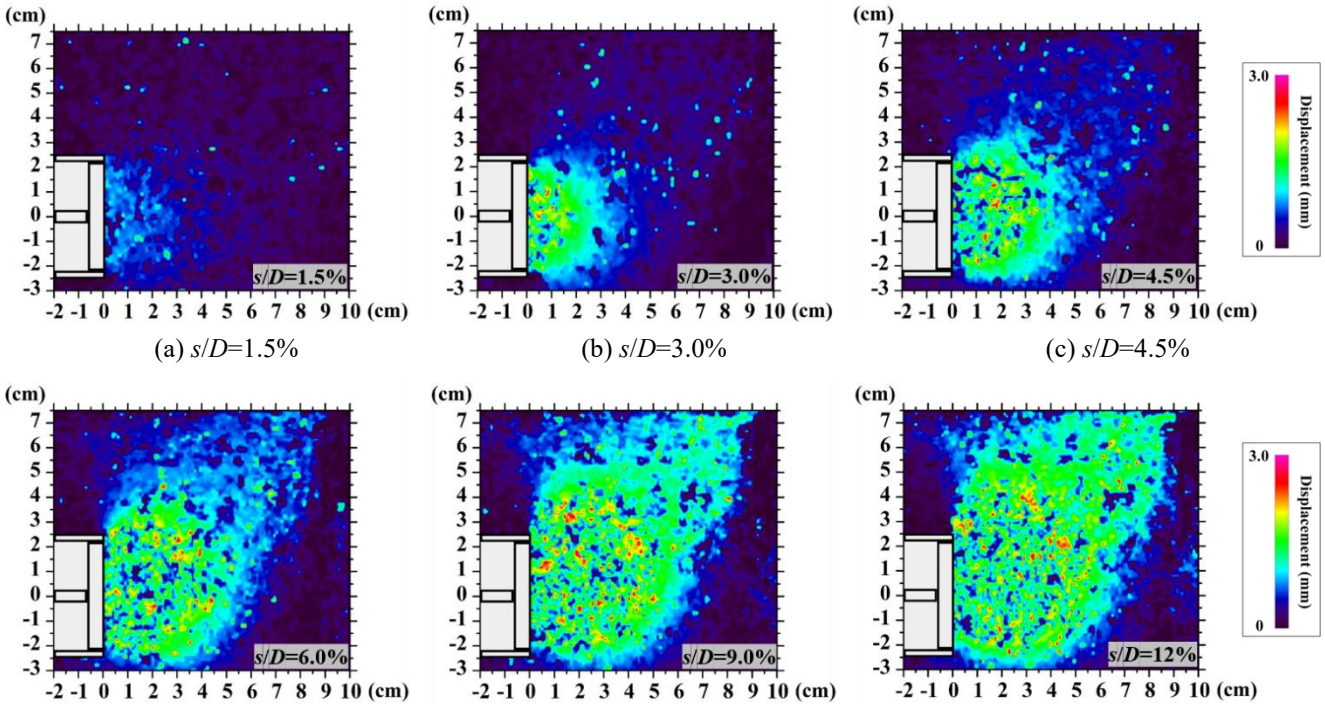

(a) s/D=1.5% (b) s/D=3.0% (c) s/D=4.5%

(d) s/D=6.0% (e) s/D=9.0% (f) s/D=12.0%

Fig. 9 The propagation process of the failure zone in the longitudinal profile (Test 3, C/D=1.0)

As shown in Table 3, in the clay layer, the retreat distance of the supporting plate reaching to the critical displacement point in this study is nearly the same as that observed by Li (2017). However, the values of p_A/p_0 and p_B/p_0 exhibit a particularly large difference. The reason for this difference is that, on the one hand, the properties of clay in this study are quite different than those in the study of Li (2017), especially the water content and cohesion, as shown in Table 1. On the other hand, the model size is different. A small full-scale model (25×25×40 m^3) is used in this study because the transparency of the TC sample decreases with the model size. However, Li (2017) conducted model tests in a semi-tunnel model box with a size of 50×60×60 m^3, the obvious adhesion between the clay and the transparent boundary hinders the changing process of the support pressure. Additionally, the limited retreat distance of the tunnel face influenced the results of the model tests conducted by Li (2017). Compared with the results of the model tests conducted in sand by Chen *et al.* (2013), the value of p_A in this study is much larger than the value of $p_{A,sand}$. The main reason for this difference is the different properties of sand and clay. The shear strength of clay is less than that of sand, which leads to a larger stress release, and the support pressure decreases slowly.

3.2 Internal soil displacement field in the longitudinal profile

3.2.1 The whole failure process in the longitudinal profile (C/D=1.0)

Fig. 9 shows the propagation process in the failure zone in the longitudinal profile, taking C/D=1.0 as an example. The failure process was a significantly progressive process. As the support pressure decreased gradually, the failure zone in front of the tunnel face developed rapidly from a small area around the tunnel face, which could be summarized as the local process. After the failure zone reached the ground, the failure process could be regarded as an integral process. The failure zone originated from the tunnel face and propagated to the ground gradually, which could be divided into the local failure process and the integral failure process. When the normalized retreat distance of the supporting plate (s/D) increased from 4.5% to 12.0%, the normalized support pressure decreased from approximately 0.3 to 0.1, and the failure zone gradually expanded from local failure to integral failure. This indicates that the displacement range and the corresponding support pressure are the critical point to ensure the construction stability of the tunnel face.

Fig. 10 shows the geometries of failure zone in the longitudinal profile. The evaluation methodology proposed

by Liu (2018) is used in this study. Two parameters, h_l and l_l are introduced to exactly describe the failure process in the longitudinal profile, where h_l is the height from tunnel crown to the top of the mainly failure zone and l_l is the width of the mainly failure zone. It must be noted that the mainly failure zone was appeared as the color of green, as shown in Fig. 9.

The h_l/C and l_l/D in the above critical displacement of Test 3 are listed in Table 4. It shows that with the retreat of the supporting plate, the h_l/C reaches to 1.0 gradually and the l_l/D reaches to 1.82. The vertical displacements are clearly smaller with respect to the horizontal ones and incline to evolve towards the upper part of the soil domain, which represented the failure process is an extension

Table 4 Parameters of failure process in the longitudinal profile

s/*D* (%)	1.5		3.0		4.5		6.0		9.0		12.0	
parameters	h_l/C	l_l/D	h_l/C	l_l/D	h_l/C	l_l/D	h_l/C	l_l/D	h_l/C	l_l/D	h_l/C	l_l/D
1.0	-	-	0.01	0.56	0.11	0.83	0.28	1.08	0.68	1.3	1.0	1.82

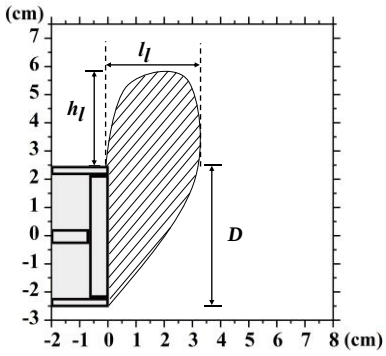

Fig. 10 Geometries of failure zone in the longitudinal profile

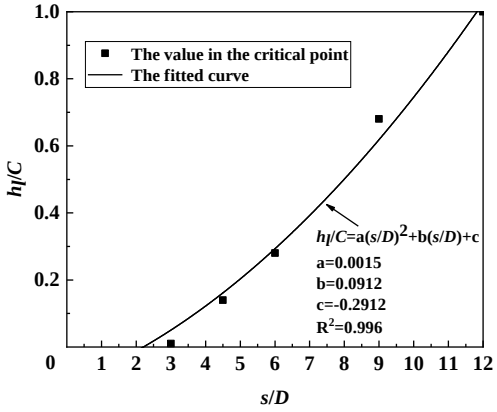

Fig. 11 The fitted curve for the failure process in the longitudinal profile

process. Due to the shearing resistance of the soil, the tunnel face maintained relatively stable when *s*/*D*=1.5%, so the parameters of this critical displacement was not listed in Table 4.

According to the above results, the failure process in the longitudinal profile can be divided more detailed. The local failure process can be divided into two stages, face deformation stage and face slip stage. In the face deformation stage (0<*s*/*D*<4.5%), the soil deformation was relatively small and mainly concentrated on the tunnel face ($h_l/C\approx0$, $l_l/D<0.8$). The face slip stage (4.5%<*s*/*D*<12%) is the most unsafety stage for construction, in which the failure zone expanded rapidly from the tunnel crown to the ground and the influence zone expanded hugely ($h_l/C<1$, $0.8<l_l/D<1.8$). After the face slip stage, the failure zone reached to the ground and the failure propagated from the local failure to the integral failure. The soil slipped to the tunnel with the retreat of the supporting plate and the failure zone spread no farther ($h_l/C=1$, $l_l/D\approx1.8$).

The parameter of h_l/C determines the ground settlement directly. The fitted result of parameters of h_l/C is shown in Fig. 11. The fitted formula was determined as $h_l/C=0.0015(s/D)^2+0.0912(s/D)-0.2912$, which can be used for the calculation of the failure process in the longitudinal profile.

3.2.2 The failure process for the critical retreat position in the longitudinal profile

Fig. 12 shows the displacement contours for the critical retreat position in the longitudinal profile. The support pressure and soil deformation induced by shield tunnelling are interrelated.

With the retreat of the supporting plate (0<*s*/*D*<4.5%), the normalized support pressure in the rapid descent stage reduced rapidly from 1.0 to approximately 0.2~0.3, and the soil around the supporting plate experienced a stage of elastoplastic deformation. The soil mass became loose, and a soil arch began to form. Meanwhile, the failure area extended up and forward. For example, when *s*/*D*=1.5%, the failure zone, which appeared as the color of the light blue, was concentrated around the tunnel face, and the soil deformation was not obvious. The shape of the failure zone was elliptical. When *s*/*D*=4.5%, the displacement contours of the soil were layered. The failure zone around the tunnel face, which appeared as the color of green, was the largest deformation region. This region could be regarded as the slip zone. The external failure zone, which appeared as the color of the light blue, could be regarded as the loose zone.

The loose zone was widely distributed, and the deformation of the edge zone was gradually reduced. The displacement contours in the centrifuge model tests showed the similar results (Calvello *et al*. 1999). The main reason for this phenomenon was the cohesion of the clay and the soil arching. At this critical point, the normalized support pressure (p/p_0) was maintained at approximately 0.2~0.3, the face stability could be retained well. This range of the support pressure was consistent with the conclusion of Zhang *et al*. (2015), but higher than the upper bound solution proposed by Leca and Dormieux (1990) for the dry Mohr-Coulomb material. The ground parameters, especially the soil properties, are the critical reason for the different critical support pressure.

With further retreat of the supporting plate (4.5%<*s*/*D*<12%), the normalized support pressure was in the slow descent stage, which reduced from 0.2~0.3 to less than 0.1. The soil deformation gradually expanded to the ground. For example, when *s*/*D*=12%, the slip zone, appeared as the color of green, reached the ground, which represented that the failure form transformed into integral displacement, in the case of *C*/*D*=0.5 and 1.0. In the case of *C*/*D*=2.0, the slip zone had a height of 1.5*D*, and the loose zone surrounded the slip zone. The failure zone could not reach the ground, and the ground settlement was not obvious.

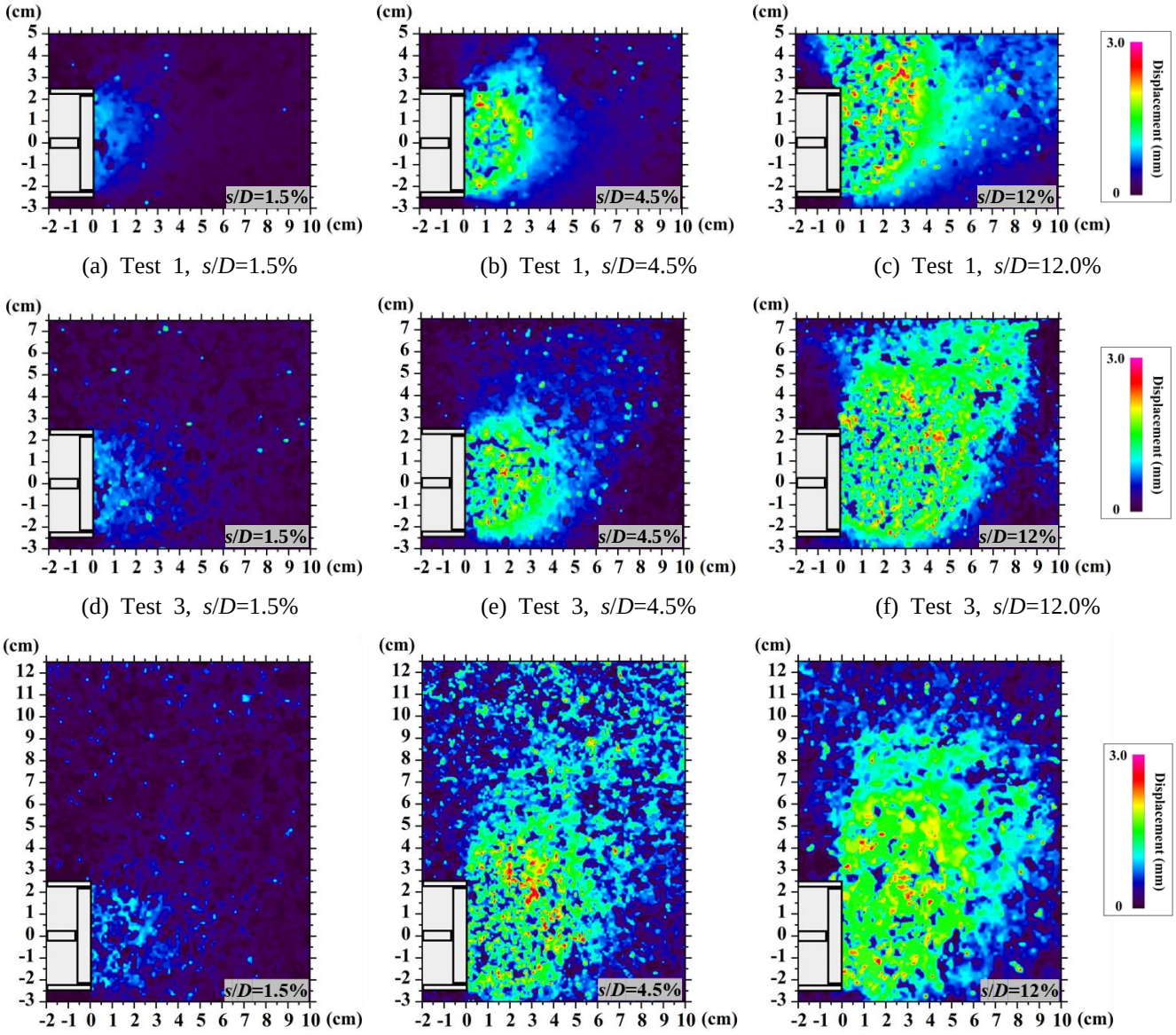

(a) Test 1, *s*/*D*=1.5% (b) Test 1, *s*/*D*=4.5% (c) Test 1, *s*/*D*=12.0%

(d) Test 3, *s*/*D*=1.5% (e) Test 3, *s*/*D*=4.5% (f) Test 3, *s*/*D*=12.0%

(g) Test 5, *s*/*D*=1.5% (h) Test 5, *s*/*D*=4.5% (i) Test 5, *s*/*D*=12.0%

Fig. 12 Displacement contours of the failure process in the longitudinal profile

At this retreat position, the buried depth had a significant influence on the failure mode of the tunnel face. In the case of *C*/*D*=0.5 and 1.0, the shear strength of the soil was fully developed. The failure mode appeared to be a basin shape, which could be divided into two parts: an ellipse in the lower part and an inverted trapezium in the upper part. However, in the case of *C*/*D*=2.0, the failure process was still a local failure process, and the shape of the main failure zone was a basin-like shape. Kirsch's tests (2010) proved that the silo had a height of roughly D_{silo} when the failure appeared in the sand. This phenomenon also existed in clay layers, even when the failure area had not reached the ground. This could explain why the support pressure reached the residual pressure in this case.

With further retreat of the supporting plate (*s*/*D*>12%), for the case of *C*/*D*=0.5 and 1.0, the support pressure was in the basic stable stage and remained at approximately 0.1, and the failure process remained the integral process. The failure zone remained the same for the case of *C*/*D*=2.0.

Fig. 13 shows the different failure mechanisms in the longitudinal profile in clay and sand. In clay, due to the cohesion, no obvious failure boundary appeared in the failure zone. The shear band could not be defined and the range of failure mode could be determined by using the displacement contour (Li *et al*. 2019b). As shown in Fig. 13(a), the failure zone expanded outward, and it could be summarized as upper wideness and lower narrowness. The upper slip surface extended outward rather than upward vertically, and the lower slip surface exhibited a logarithmic curve rather than a wedge shape. However, as shown in Figs. 13(b) and 13(c) the failure zone propagated vertically towards the ground in sand layers. The failure zone could be divided into a wedge in the lower part and a silo in the upper part, in which the slip surface was vertical (Lv *et al.*

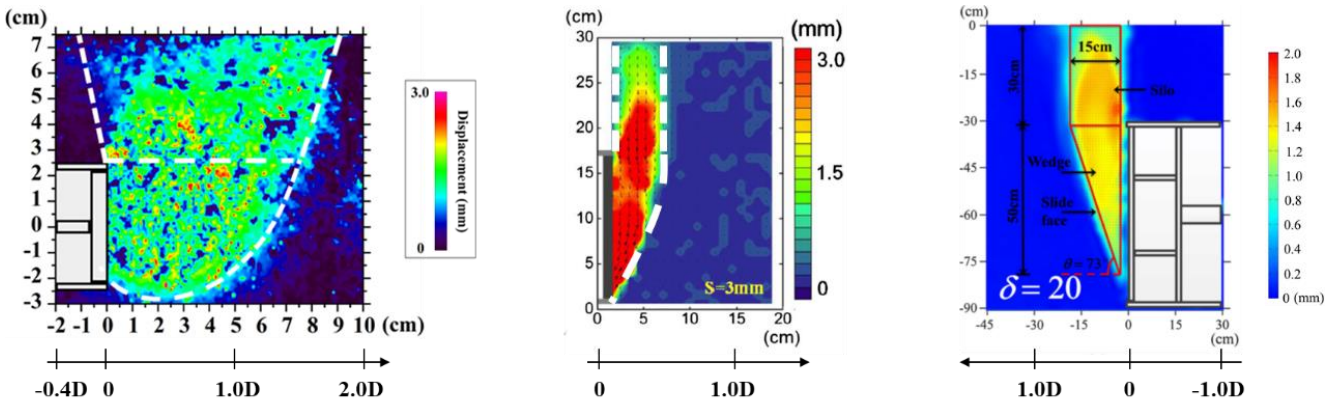

(a) Clay (this study) (b) Sand (Lv *et al.* 2018) (c) Sand (Liu *et al.* 2018)

Fig. 13 The different failure mechanisms in clay and sand (longitudinal profile)

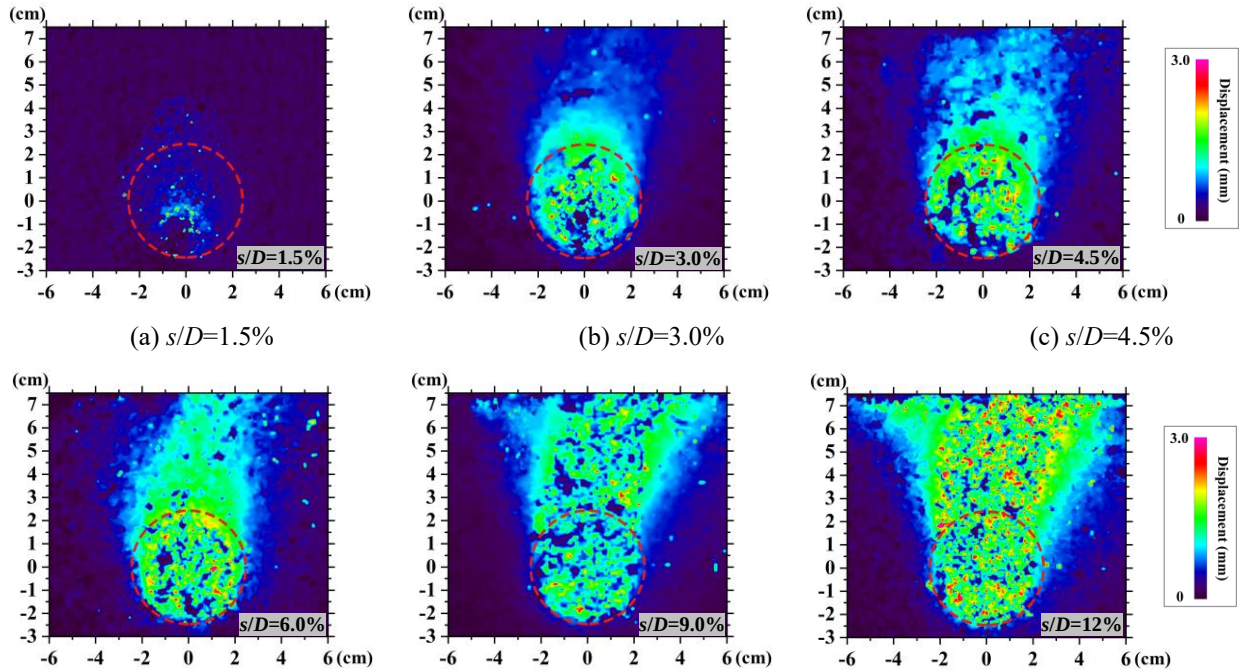

(a) *s*/*D*=1.5% (b) *s*/*D*=3.0% (c) *s*/*D*=4.5%

(d) *s*/*D*=6.0% (e) *s*/*D*=9.0% (f) *s*/*D*=12.0%

Fig. 14 The propagation process of the failure zone in the cross profile (*C*/*D*=1.0)

2018, Liu *et al.* 2018). As a result, the range of the failure zone in clay is much larger than that in sand.

3.3 Internal soil displacement field in the cross profile

3.3.1 The whole failure process in the cross profile (C/D=1.0)

Fig. 14 shows the propagation process in the failure zone in the cross profile, taking *C*/*D*=1.0 as an example. The failure process was a significantly progressive process that expanded to the ground gradually, and was accompanied by the occurrence of the soil arching effect. These results are consistent with the failure process in the longitudinal profile.

The evaluation methodology used in the longitudinal profile is redefined to describe the failure process in the cross profile, as shown in Fig. 15, where h_c is the depth from tunnel crown to the top of the mainly failure zone, l_c is the widest region of the mainly failure zone.

The h_c/C, l_c/D in the above critical displacement of Test 4 are listed in Table 5. At the same retreat displacement, the parameter of l_c/D in the cross profile is larger than the parameter of l_l/D, which means that the transverse failure zone is larger than the longitudinal failure zone.

The failure stage presented in section *3.2* can also be certified. The soil deformation during the face deformation stage was mainly concentrated on the tunnel face ($h_c/C\approx0$, $l_c/D<0.8$). In the face slip stage ($4.5\%<s/D<12\%$), the soil deformation expanded to the ground and the scope of the influence zone was widespread ($h_c/C<1$, $1.0<l_c/D<2.4$). Then the failure zone propagated into the integral failure and the failure zone no further increase ($h_c/C=1$, $l_c/D\approx2.4$).

Table 5 Parameters of failure process in the cross profile

s/D (%)	1.5		3.0		4.5		6.0		9.0		12.0	
parameters	h_c/C	l_c/D	h_c/C	l_c/D	h_c/C	l_c/D	h_c/C	l_c/D	h_c/C	l_c/D	h_c/C	l_c/D
1.0	-	-	0.07	0.86	0.16	1.0	0.38	1.06	0.84	1.6	1.0	2.4

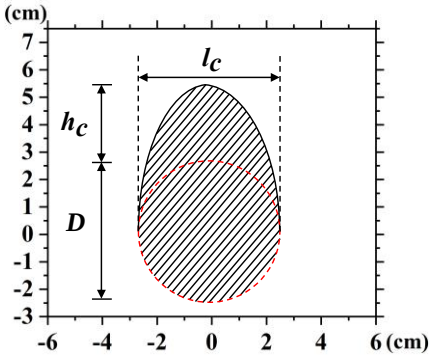

Fig. 15 Geometries of failure zone in the cross profile

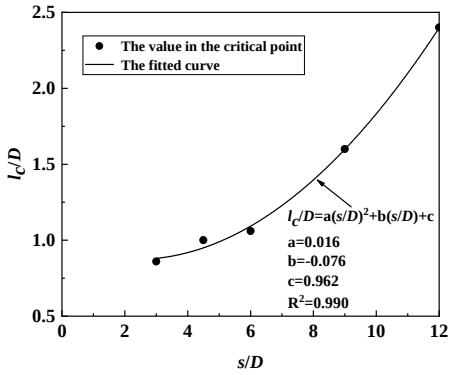

Fig. 16 The fitted curve for the failure process in the cross profile

The fitted result of l_c/C is shown in Fig. 16. The fitted formula l_c/C =0.016$(s/D)^2$-0.076(s/D)+0.962 (R^2=0.990) can be used for the calculation of the failure process in the cross profile.

3.3.2 The failure process for the critical retreat position in the cross profile

Fig. 17 shows the displacement contours of the critical retreat position in the cross profile.

When s/D=1.5%, a loose zone appeared on the tunnel face under each C/D, representing the beginning of failure. When s/D=4.5%, the failure zone could be divided into a slip zone and a loose zone. The slip zone concentrated at the tunnel face. When s/D=12%, in the case of C/D=0.5 and 1.0, the failure zone reached the ground.

The final failure zone formed the shape of an inverted trapezoid. This shape is very different from the failure shape in sand, in which the upper part is a rectangle (Sun *et al.* 2014). In the case of C/D=2.0, the failure shape was a teardrop-like shape. However, in sand the upper part exhibited a bell shape (Sun *et al.* 2014).

Fig. 18 shows the different failure mechanisms in clay and sand. In the clay layer, there was no obvious failure boundary, and the loose area was extensive. The slip surface was an outward expanding slip surface, which could prove the conclusion of Mair and Taylor (1997). The influence zone started at the tunnel spring line and formed an angle of 68° with the horizontal side in this study, which was larger than the angle of 47° in sand. This also resulted in the difference in the failure mechanisms in clay and sand.

4. Conclusions

A series of transparent clay (TC) model tests have been conducted to investigate the relationship between the support pressure and the internal soil movements. The soil movement characteristics of each failure stage in the failure process are defined. The failure mechanism in different layers, different buried depths and different profiles are compared and specified. Based on the results of the model tests, the following conclusions can be drawn:

- The reliability of the TC model test is verified by comparing the geotechnical properties of TC and natural clay. With the help of visualization of transparent clay, the internal soil movements under different buried depths and different profiles were analysed. The non-intrusive and continuous measurement can be realized.

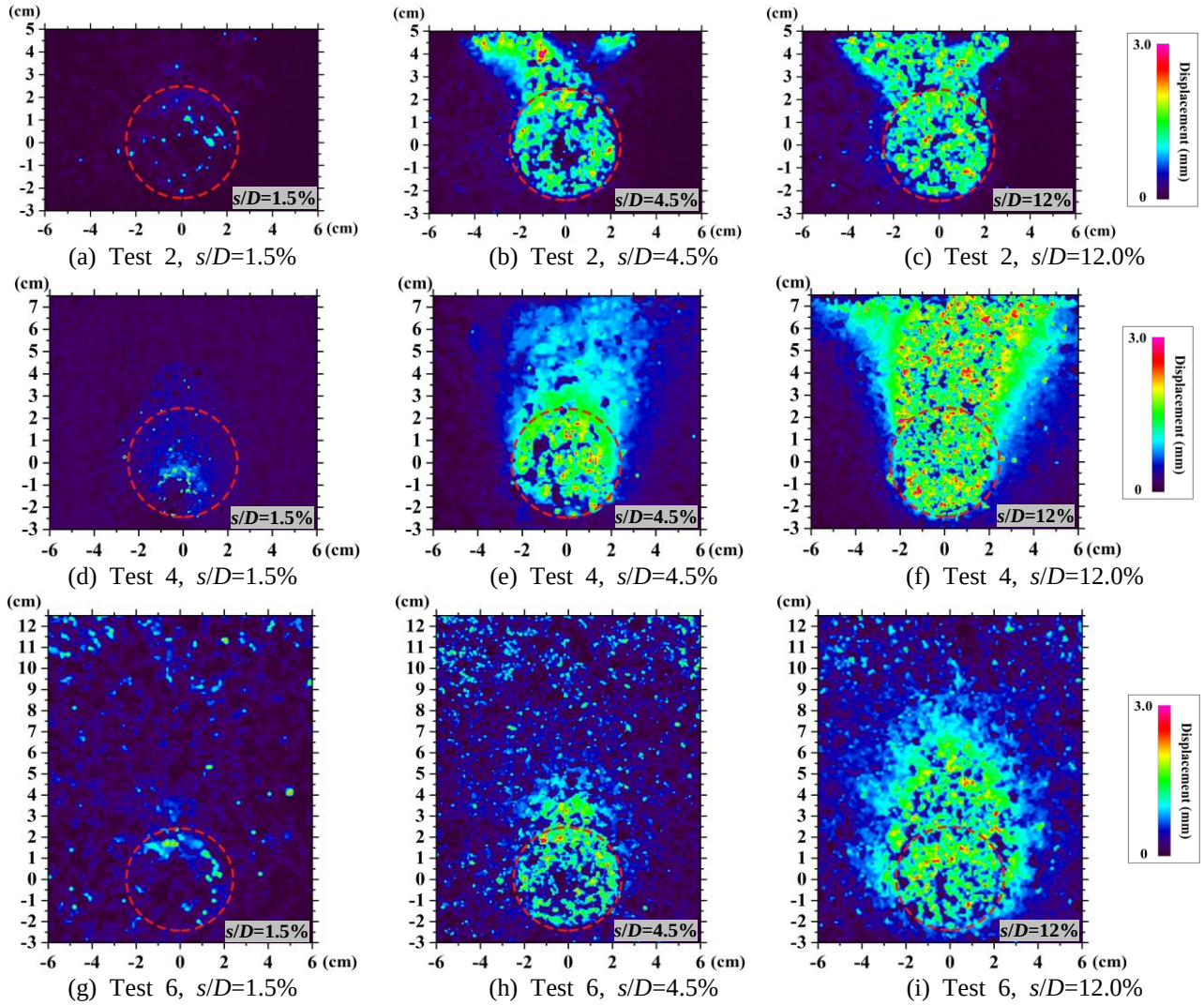

(a) Test 2, *s*/*D*=1.5% (b) Test 2, *s*/*D*=4.5% (c) Test 2, *s*/*D*=12.0%

(d) Test 4, *s*/*D*=1.5% (e) Test 4, *s*/*D*=4.5% (f) Test 4, *s*/*D*=12.0%

(g) Test 6, *s*/*D*=1.5% (h) Test 6, *s*/*D*=4.5% (i) Test 6, *s*/*D*=12.0%

Fig. 17 Displacement contours of the failure process in the cross profile

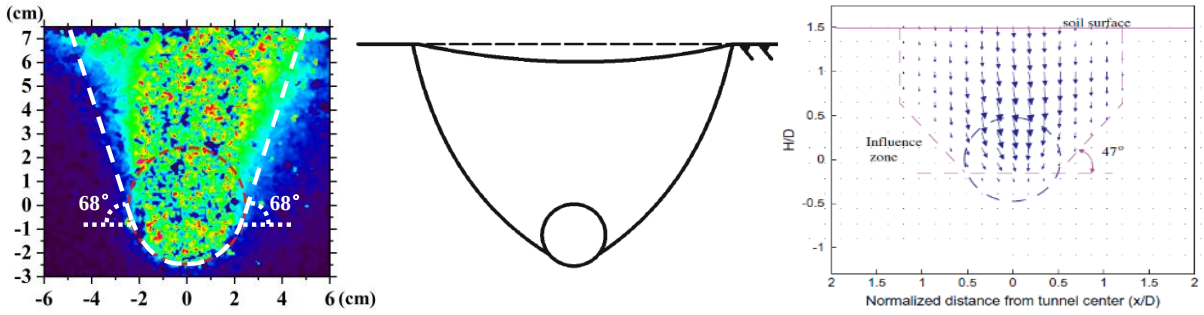

(c) Sand (Sun *et al.* 2014)

Fig. 18 The different failure mechanism in clay and sand (cross profile)

- The changing process of the support pressure in clay is specified into three stages: rapid descent stage, slow descent stage and the basically stable stage. The normalized support pressure in each critical point is specified. Compared with that in sand, the changing process of the support pressure in clay is sluggish.
- From the view of the internal soil movements, the failure zone can be divided into the slip zone and the loose zone. With the retreat of the supporting plate, the soil of the slip zone rushed into the tunnel and the surrounding soil of the loose zone was disturbed and loosed continuously to the ground. The fitted formulas are proposed for the calculation of the failure process.
- The failure process is a propagation process, which can be divided into the local failure ($0 < s/D < 1$ 2%) and the integral failure ($s/D > 12\%$). In the case of C/D=0.5 and 1.0, the failure mode appears as the basin shape in the longitudinal profile and an inverted trapezoid in the

cross profile. In the deep case, the failure mode appears the same shape in the longitudinal profile but appears as a teardrop-like shape in the cross profile. The failure zone did not react the ground, owing to the soil arching.

It is important to note that some limitations existed in this study. Because the transparency of transparent clay decreases with increasing thickness, only small-scale model tests were conducted at a gravity condition. The stress state of the natural soil could not be fully reflected and the scale effect was significant, so the results of this study could not be applied to field performance in directly, as proposed by Sun *et al.* (2014). The tunnel was pre-buried and the effect of the excavation process was not considered in the test. Meanwhile, only the plane (2D) displacement field under different profiles was studied in this paper. The full 3D displacement field should be measured to study the failure mechanisms in further studies.

Acknowledgments

The authors acknowledge the National Key Research and Development Program of China (Grant No. 2017YFC0805402), the Open Project of State Key Laboratory of Disaster Reduction in Civil Engineering (Grant No. SLDRCE17-01), the Tianjin Research Innovation Project for Postgraduate Students (Grant No. 2021YJSB141) for funding this work.

References

Ads, A., Iskander, M. and Bless, S. (2020), "Soil–projectile interaction during penetration of a transparent clay simulant", *Acta Geotech.*, **15**(4), 815-826. https://doi.org/10.1007/s11440-020-00921-z.

Ahmed, M. and Iskander, M. (2011), "Analysis of tunneling-induced ground movements using transparent soil models", *J. Geotech. Geoenviron.*, **137**(5), 525-535. https://doi.org/10.1061/(ASCE)GT.1943-5606.0000456.

Ahmed, M. and Iskander, M. (2012), "Evaluation of tunnel face stability by transparent soil models", *Tunn. Undergr. Sp. Tech.*, **27**(1), 101-110. https://doi.org/10.1016/j.tust.2011.08.001.

Alagha, A.S. and Chapman, D.N. (2019), "Numerical modelling of tunnel face stability in homogeneous and layered soft ground", *Tunn. Undergr. Sp. Tech.*, **94**, 103096. https://doi.org/10.1016/j.tust.2019.103096.

Azadi, M., Ghasemi, S.H. and Mohammadi, M. (2020), "Reliability analysis of tunnels with consideration of the earthquakes extreme events", *Geomech. Eng.*, **22**(5), 433-439. https://doi.org/10.12989/gae.2020.22.5.433.

Berthoz, N., Branque, D., Subrin, D., Wong, H. and Humbert, E. (2012), "Tunneling in stratified soft ground: Experimental study on 1g EPBS reduced scale model", Geotechnical Aspects of Underground Construction in Soft Ground – Proceedings of the 7th International Symposium on Geotechnical Aspects of Underground Construction is Soft Ground, 411-416.

Calvello, M. and Taylor, R.N. (1999), "Centrifuge modelling of a pile-reinforced tunnel heading", Proceedings of geotechnical aspect of underground construction in soft rock, Rotterdam, 313-318.

Chen, R.P., Li, J., Kong, L.G. and Tang, L.J. (2013), "Experimental study on face instability of shield tunnel in sand", *Tunn. Undergr. Sp. Tech.*, **33**, 12-21. https://doi.org/10.1016/j.tust.2012.08.001.

De Guzman, E.M.B. and Alfaro, M.C. (2018), "Laboratory-scale model studies on corduroy-reinforced road embankments on peat foundations using transparent soil", *Transp. Geotech.*, **16**, 1-10. https://doi.org/10.1016/j.trgeo.2018.05.002.

di Prisco, C., Flessati, L., Frigerio. G. and Lunardi, P. (2018a), "A numerical exercise for the definition under undrained conditions of the deep tunnel front characteristic curve", *Acta Geotech.*, **13**(3), 635-649. https://doi.org/10.1007/s11440-017-0564-y.

di Prisco, C., Flessati, L., Frigerio. G., Castellanza, R., Caruso, M. Galli, A. and Lunardi, P. (2018b). "Experimental investigation of the time-dependent response of unreinforced and reinforced tunnel faces in cohesive soils", *Acta Geotech.*, **13**(3), 651-670. https://doi.org/10.1007/s11440-017-0573-x.

Eskandari, F., Goharrizi, K.G. and Hooti, A. (2018), "The impact of EPB pressure on surface settlement and face displacement in intersection of triple tunnels at Mashhad metro", *Geomech. Eng.*, **15**(2), 769-774. https://doi.org/10.12989/gae.2018.15.2.769.

Fernandez, F., Rojas, J.E.G., Vargas, E.A., Velloso, R.Q. and Dias, D. (2021), "Three-dimensional face stability analysis of shallow tunnels using numerical limit analysis and material point method", *Tunn. Undergr. Sp. Tech.*, **112**. https://doi.org/10.1016/j.tust.2021.103904.

Guzman, I., Iskander, M. and Bless, S. (2019), "A comparison of half and quarter space penetration into granular media", *Geotech. Test. J.*, **43**(4), 809-828. https://doi.org/10.1520/GTJ20190080.

Horpibulsuk, S., Phetchuay, C., Chinkulkijniwat, A. and Cholaphatsorn, A. (2013), "Strength development in silty clay stabilized with calcium carbide residue and fly ash", *Soils Found.*, **53**(4), 477-486. https://doi.org/10.1016/j.sandf.2013.06.001.

Iskander, M. (2010), "Modelling with transparent soils: visualizing soil structure interaction and multi phase flow, non-intrusively", Springer Science & Business Media, Berlin, Germany.

Iskander, M.G., Liu, J.Y. and Sadek, S. (2002). "Transparent amorphous silica to model clay". *J. Geotech. Geoenviron. Eng.*, **128**(3), 262-273. https://doi.org/10.1061/(ASCE)1090-0241(2002)128:3(262).

Juneja, A., Hegde, A., Lee, F.H. and Yeo, C.H. (2010), "Centrifuge modelling of tunnel face reinforcement using forepoling", *Tunn. Undergr. Sp. Tech.*, **25**(4), 377-381. https://doi.org/10.1016/j.tust.2010.01.013.

Kamata, H. and Mashimo, H. (2003), "Centrifuge model test of tunnel face reinforcement by bolting", *Tunn. Undergr. Sp. Tech.*, **18**(2), 205-212. https://doi.org/10.1016/S0886-7798(03)00029-4.

Kim, Y.W. and Lee, S.D. (2016), "Experimental study on the longitudinal load transfer of a shallow tunnel depending on the deformation tunnel face", *J. Korean Tunn. Undergr. Sp. Asso.*, **18**(5), 487-497. https://doi.org/10.9711/KTAJ.2016.18.5.487.

Kimura, T. and Mair, R.J. (1981), "Centrifugal testing of model tunnels in soft clay", In: Proceedings of the 10th international conference on soil mechanics and foundation engineering (pp. 319-322). ISSMFE: International Society for Soil Mechanics and Foundation Engineering.

Kirsch, A. (2010), "Experimental investigation of the face stability of shallow tunnels in sand", *Acta Geotech.*, **5**(1), 43-62. https://doi.org/10.1007/s11440-010-0110-7.

Kong, G.Q., Li, H., Yang, G. and Cao, Z.H. (2018), "Investigation on shear modulus and damping ratio of transparent soils with different pore fluids", *Granul. Matter*, **20**(1), 1-8. https://doi.org/10.1007/s10035-017-0779-5.

Leca, E. and Dormieux, L. (1990), "Upper and lower bound solutions for the face stability of shallow circular tunnels in frictional material", *Geotechnique*, **40**(4), 581–606. https://doi.org/10.1680/geot.1990.40.4.581.

Lei, H.Y., Liu, Y.N. and Zhai, S.B. (2019), "Study on visibility

and mechanical properties of transparent clay", *Chinese J. Geotech. Eng.*, **41**(S2), 53-56. https://doi.org/10.11779/CJGE2019S2014.

Lei, H.Y., Ren, Q., Lu, H.B. and Li, B. (2018). "Research on consolidation property of double layer soft clay foundation under different relative thickness conditions", *Chinese J. Undergr. Sp. Eng*., **14**(3), 705-711. https://doi.org/CNKI:SUN:BASE.0.2018-03-020.

Li, J.Y. (2017), "Model test and theoretical studies on face instability of shallow shield tunnel", M.S. Dissertation, Zhejiang University, Hangzhou, China.

Li, T.Z. and Yang, X.L. (2019a), "Face stability analysis of rock tunnels under water table using Hoek-Brown failure criterion", *Geomech. Eng.*, **18**(3), 235-245. https://doi.org/10.12989/gae.2019.18.3.235.

Li, W., Zhang, C., Zhu, W. and Zhang, D. (2019b), "Upper-bound solutions for the face stability of a non-circular natm tunnel in clays with a linearly increasing undrained shear strength with depth", *Comput. Geotech.*, **114**, 103136. https://doi.org/10.1016/j.compgeo.2019.103136.

Li, W., Zhang, C.P., Tan, Z.B. and Ma, M.S. (2021), "Effect of the seepage flow on the face stability of a shield tunnel", *Tunn. Undergr. Sp. Tech*., **112**(4), 103900. https://doi.org/10.1016/j.tust.2021.103900.

Liu, H.H., Zhong, H.Y., Gu, X., Xiang, Y.Z. and Zhang, W.G. (2021). Transparent soil model testing on ground settlement induced by parallel tunnels excavation. *J. Civil Environ Eng*., **43**(1), 1-10. https://doi.org/10.11835/j.issn.2096-6717 2020.0821.

Liu, W., Zhao, Y., Shi, P.X., Li, J.Y. and Gan, P.L. (2018), "Face stability analysis of shield-driven tunnels shallowly buried in dry sand using 1-g large-scale model tests", *Acta Geotech.*, **13**(3), 693-705. https://doi.org/10.1007/s11440-017-0607-4.

Lv, X.L., Zhou, Y.C., Huang, M.S. and Zeng, S. (2018), "Experimental study of the face stability of shield tunnel in sands under seepage condition", *Tunn. Undergr. Sp. Tech*., **74**, 195-205. https://doi.org/10.1016/j.tust.2018.01.015.

Mohidin, N., Alfaro, M. and Masirin, M. (2010), "Development of transparent clay for laboratory model tests", *GEO2010*, Calgary, AB, Canada.

Nomoto, T., Imamura, S., Hagiwara, T., Kusakabe, O. and Fujii, N. (1999), "Shield tunnel construction in centrifuge", *J. Geotech. Geoenviron. Eng.*, **125**(4), 289-300. https://doi.org/10.1061/(ASCE)1090-0241(1999)125:4(289).

Sahoo, J.P. and Kumar, B. (2019), "Stability of circular tunnels in clay with an overlay of sand", *Int. J. Geomech*., **19**(3), 06018039. https://doi.org/10.1061/(ASCE)GM.1943-5622.0001360.

Senent, S., Yi, C.K. and Jimenez, R. (2020), "An upper bound solution for tunnel face stability analysis considering the free span", *Tunn. Undergr. Sp. Tech*., **103**, 103515. https://doi.org/10.1016/j.tust.2020.103515.

Shin, J.H., Choi, Y.K., Kwon, O.Y. and Lee, S.D. (2008), "Model testing for pipe-reinforced tunnel heading in a granular soil", *Tunn. Undergr. Sp. Tech*., **23**(3), 241-250. https://doi.org/10.1016/j.tust.2007.04.012,

Sun, J.Z. and Liu, J.Y. (2014), "Visualization of tunnelling-induced ground movement in transparent sand", *Tunn. Undergr. Sp. Tech*., **40**, 236-240. https://doi.org/10.1016/j.tust.2013.10.009.

Vermeer, P.A., Ruse, N. and Marcher, T. (2002), "Tunnel heading stability in drained ground", Felsbau, **20**(6), 8-18.

Wang, B., Hou H.J., Zhut, Z.W. and Xiao, W. (2021), "Machine learning-based prediction and performance study of transparent soil properties", *Smart Struct. Syst.*, **28**, 289-304. https://doi.org/10.12989/sss.2021.28.2.289.

Xiang, Y.Z., Liu, H.L., Zhang, W.G., Chu, J., Zhou, D. and Xiao, Y. (2018), "Application of transparent soil model test and DEM simulation in study of tunnel failure mechanism", *Tunn. Undergr. Sp. Tech*., **74**, 178-184. https://doi.org/10.1016/j.tust.2018.01.020.

Xue, Y.G., Li, X., Qiu, D.H., Ma, X.M., Kong, F.M., Qu, C.Q. and Zhao, Y. (2019), "Stability evaluation for the excavation face of shield tunnel across the Yangtze River by multi-factor analysis", *Geomech. Eng.*, **19**(3), 283-293. https://doi.org/10.12989/gae.2019.19.3.283.

Zhang, C., Han, K. and Zhang, D. (2015), "Face stability analysis of shallow circular tunnels in cohesive–frictional soils". *Tunn. Undergr. Sp. Tech.*, **50**, 345-357. https://doi.org/10.1016/j.tust.2015.08.007.

Zhang, W., Gu, X., Zhong, W., Ma, Z. and Ding, X. (2020a). "Review of transparent soil model testing technique in underground construction: ground visualization and result digitalization", *Undergr Sp.*, (1). https://doi.org/10.1016/j.undsp.2020.05.003.

Zhang, W., Zhong, H., Xiang Y., Wu, D., Zeng, Z. and Zhang, Y. (2020b), "Visualization and digitization of model tunnel deformation via transparent soil testing technique", *Undergr. Sp.*, (1). https://doi.org/10.1016/j.undsp.2020.05.004.

Zhang, Z., Tao, F.J., Han, J., Ye, G.B., Cheng, B.N. and Liu, L. (2020c), "Influence of surface footing loading on soil arching above multiple buried structures in transparent sand", *Can. J. Civil. Eng*., **48**(2).

CC